Robotica (2012) volume 30, pp. 123–132. © Cambridge University Press 2011
doi:10.1017/S026357471100035X

Trajectory estimation of a skid-steering mobile robot propelled by independently driven wheels

Tokuji Okada*, Abeer Mahmoud, Wagner Tanaka Botelho and Toshimi Shimizu

Information Science and Engineering, Graduate School of Science and Technology, Niigata University, Niigata 950-2181, Japan

(Received in Final Form: March 18, 2011. First published online: May 6, 2011)

SUMMARY

This paper analyses a mobile robot with independently rotating wheels travelling on uneven but smooth ground, including ascending or descending surfaces. We formulate a mathematical expression for the energy cost of the robot's movement. For our analysis, we utilise the principle of virtual work and assume that the robot moves with a fixed arrangement of wheel axes and without using a steering handle. The mathematical model reveals that the coefficient of friction and the payload distribution dominate the wheel behaviour, including slipping and skidding. We minimise the virtual work expression to determine the robot's motion complying with driven wheels. The model also enables us to estimate trajectories for different ground conditions. A hybrid robot, PEOPLER-II, is used to demonstrate the predicted motions, including turns and spins, by following angular velocity control rules. Experimental data verifies that the proposed formulation and minimisation of virtual work are valid techniques for predicting a robot's trajectory. The method described is widely applicable to wheeled robots having independently driven wheels.

KEYWORDS: Wheeled robot; Trajectory estimation; Virtual work; Coefficient of friction; Payload distribution.

1. Introduction

Mobile robots using conventional tyres are popular for moving quickly over a flat terrain. There are many types of wheels based on the mechanisms that support loads and transmit power for driving robots: these wheels vary in terms of elasticity of the circumferential material and gripping performance on the ground. Wheels, such as casters, omnidirectional wheels, rimless wheels, spherical balls, skid wheels and mecanum wheels, have been commercialised thus far.[1] Most four-wheeled mobile robots use two wheels as steerable wheels or differential driving wheels.[2] The other two wheels are typically free wheels[3] or caster wheels.[4] However, the mobile robot KAMRO changes its direction of travel by controlling four omnidirectional wheels. Wheel slipping and skidding influence the control necessary for a robot to accurately follow a given trajectory.[5]

* Corresponding author. E-mail: okada@eng.niigata-u.ac.jp

A previous study proposed a dynamic model for a four-wheel differentially driven mobile robot that takes into account the effects of wheel skidding.[6] Other authors have presented kinematic models that explicitly relate perturbations to vehicle slipping and skidding.[7] Meanwhile, in a traction model for wheeled robots,[8] the adhesion coefficient between the wheels of a wheeled mobile robot and a hard flat surface was calculated as a function of wheel slip. In another study, the total amount of wheel rotation was optimised for differentially driven mobile robots to achieve the shortest path.[9] In a similar study, mobile robots with two independently driven wheels were used to generate a time-optimal trajectory.[10] Finally, rigid differentially steered axles were coupled to a compliant frame module to make a four-wheeled robot stand stably on a rough terrain.[11] The absence of an explicit steering assembly makes four-wheel drive skid-steering mobile robot (4WDSSMRs) mechanically robust and able to move on rough terrain with ease and good manoeuvrability as an all-terrain response vehicle. However, most dynamic models are limited in predicting the motion of 4WDSSMRs because the models are typically not applicable to a variety of ground conditions. Therefore, an effective and simple calculation method for visualizing the motion of 4WDSSMRs needs to be developed.

The focus of this paper is to analyse the behaviour of skid-steering wheels to estimate the trajectory of a robot. In our analysis, the robot has independently rotating wheels with a simple control scheme as in our previous study.[12] For the convenience of verifying model predictions using the hybrid robot PEOPLER-II,[13] we consider a robot having four nonsteerable wheels at the ends of parallel aligned front and rear axes. Each wheel is set to have the same radius. In the analysis, we take into account such factors as the coefficient of friction, the weight distribution operating at the wheel contacts, wheel rotation speed, gravitational potential and the aspect ratio of the body frame.

Motivation of the trajectory estimation is to generate a control input of 4WDSSMRs for satisfying driver's requests, i.e. control of a propelling direction, to follow a path to a destination by a standardised coarse manoeuvring as if drivers move with a feeling of controlling on an ordinary terrain. For developing the manoeuvring system, an ordinary control input necessitates revision using an appropriate function of calibration so that the robot moves in real world even when a position of the centre of gravity (COG) and a

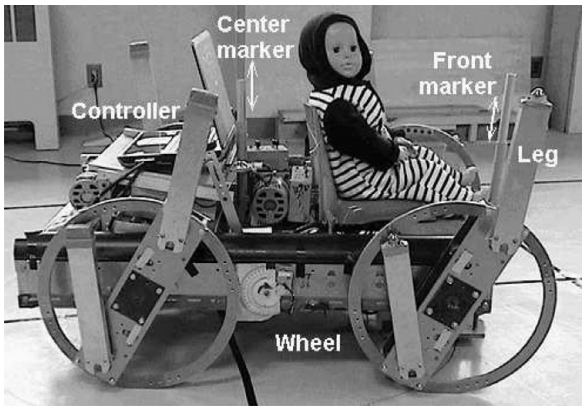

Fig. 1. Hybrid robot PEOPLER-II configured for wheeled locomotion.

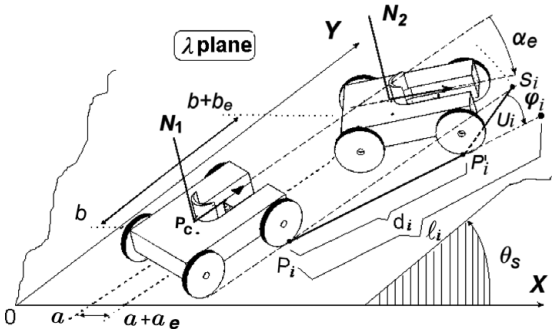

Fig. 2. Robot posture before and after a small displacement on a slope.

road-type, including inclination change. The position of COG might be roughly modified by checking a loaded direction of a burden on a platform of the robot. Inclination of a road surface might be given by a two-axis direction sensor and the coefficient of friction will be assigned by drivers because they can recognise what type of road is on the way as a visual information. Collection of this occasional information makes it possible to determine an appropriate control input by calculating functions that might be formulated by using simulation results in advance.

We simulate the robot motion using our mathematical model to estimate the robot's trajectory and then verify the predicted trajectory by comparing it to experimental data. In Section 2, we show a typical robot postures before and after a small displacement to define the parameters of interest. In Section 3, we formulate our mathematical analysis for estimating the energy cost of a small motion. The procedure for minimizing the energy cost is presented in Section 4. Section 5 presents a simulation of steering by turning and spinning for visualizing a robot trajectory. In Section 6, experimental results using the PEOPLER-II are shown to verify the simulation results. Finally, in Section 7, we present the concluding remarks.

2. Robot Postures Before and After a Small Movement

In 4WDSSMRs, the motion of a turn or a spin is produced by changing the angular velocity of each wheel independently, i.e. without installing a steering mechanism. The difference in wheel speeds creates the steering motion. Thereby, the motion of 4WDSSMRs is influenced by slipping and skidding of each wheel on the ground. These are undesirable from energy saving viewpoint, but inevitable and essential to make the robot change its direction of travel. Robots, such as *GAIA, Khepera* and *Koala*, are commercially available. Our robot, PEOPLER-II, is a 4WDSSMR when configured to operate as a wheel-type (see Fig. 1).[14] Note that the PEOPLER-II robot's body is not rigid, and thus, it can stand on rough terrain with four wheels in contact with ground. Figure 2 shows the three-dimensional movement of a 4WDSSMR on a slope. In the figure, the robot platform is parallel to the ground surface, in general. The symbols N_1 and N_2 denote the normals to the robot platform before and after a small displacement, respectively. Other symbols and parameters for the motion analysis are as follows:

(a, b) : X and Y components of a cross point of the normal N_1 on the ground in Σ_0 and Σ.
(a_e, b_e): X and Y components of a small displacement of the normal for moving from N_1 to N_2 in Σ_0 and Σ.
i: subscript related to a wheel position ($i = 1 - 4$).
d_i : translational wheel displacement, i.e. $\overline{P_i P_i'}$.
i : subscript related to a wheel position ($i =$ 1–4).
l_i: rolling distance of a wheel within Δt in the case when there is no obstruction.
A_i : tread area (width; t_{ai}, length; t_{bi}).
L_h: length between axes.
L_w: width between wheels.
P_i : ith wheel contact on the ground.
P_0 : vertical projection of P_c on the plane of ζ and ζ_0.
P_5 : imaginary point where the resultant load at P_1 and P_2 operates.
P_6 : cross point of the line η with the vertical plane, including P_1 and P_2.
P_7 : vertical projection of P_g(COG) on the $X_0 - Y_0$ plane.
P_c : geometrical centre of a robot body.
$P_{i0}(x_{i0}; y_{i0}; z_{i0})$: initial wheel position on ζ_0 in Σ_0.
$P_{0i}(x_{0i}; y_{0i}; z_{0i})$: actual wheel position on ζ in Σ after a small movement of the robot.
$S_i(x_{si}; y_{si}; z_{si})$: imaginary wheel position on ζ in Σ when the wheel rolls straight forward by a small angular displacement without any disturbance.
R_i : wheel radius.
SMC : span of marker-C's trajectory ($\mathrm{SMC_{max}}$, $\mathrm{SMC_{min}}$).
SMF : span of marker-F's trajectory ($\mathrm{SMF_{max}}$, $\mathrm{SMF_{min}}$).
U_i : untrodden virtual distance between P_i' and S_i.
W_{i0}: load operating at a wheel contact on $\zeta_0 (i = 1 - 5, 7)$.
W_i : load operating at a wheel contact on ζ.
α: angular shift of the robot's direction from an initial direction, i.e. direction of Y-axis.
α_e : angular displacement of α within a small displacement of the robot.
η: virtual body axis extending straight forward parallel from P_c internally around which the front body twists freely to have four wheels in contact with the ground.
θ_i : wheel rotation angle.

https://doi.org/10.1017/S026357471100035X Published online by Cambridge University Press

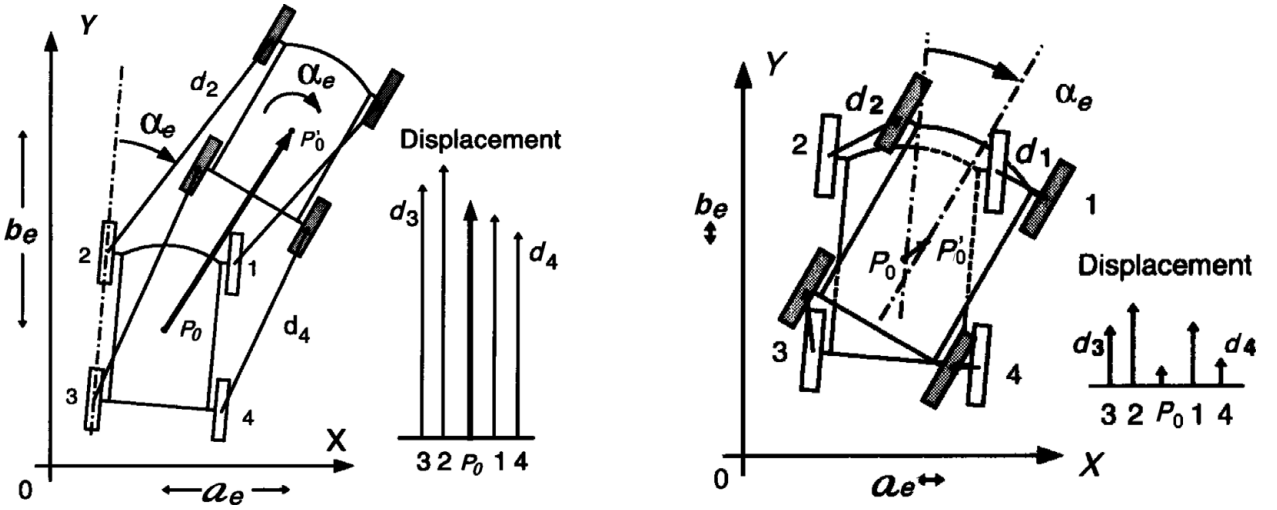

Fig. 3. Microscopic displacements of four wheels in a short time on the plane λ. Motions of a turn and a spin are in the left and right parts, respectively. Displacements of $d_i (i = 1 - 4)$ in each motion are compared in a bar graph.

θ_s : inclination angle of the ground surface.
μ_i : coefficient of friction (μ_{si}: static, μ_{di}: dynamic).
v_i : rolling speed of a wheel.
ω_i : angular velocity of a wheel (ω_l: left, ω_r: right).
ρ: radius of curvature.
λ_v: ratio of ω_l to $\omega_r (= v_l / v_r)$.
ζ_0 : horizontal home ground of a robot standing, i.e. the $X_0 - Y_0$ plane of Σ_0 before a coordinate transformation.
ζ: surface of the actual ground, i.e. the X–Y plane of Σ generated after a coordinate transformation of Σ_0 with θ_s around the X_0-axis.
Σ_0 : coordinate system of the horizontal home ground.
Σ: coordinate system of the ground inclined at θ_s.

The left part of Fig. 3 shows a magnified top view of possible wheel positions before and after a small displacement for the wheel to turn on ζ. Each of the rolling trajectories produced by the small angular shift may be a curve. However, we suppose that the trajectory is linear due to the smallness of the shift. Clearly, each is different in length from the other. Also, each of the wheel directions must produce an angular displacement similar to that of the robot body. In fact, all the wheel displacements are the same, and α_e is zero when the robot rolls straight forward without disturbance. Likewise, the wheel positions corresponding to a robot spinning before and after a small displacement are illustrated in the right part of Fig. 3. Spinning motion has the property that linear translation of the robot body is relatively small, but the angular displacement is relatively large owing to the opposite directions of turning of the right and left wheels.

3. Analysis of Vehicular Movement

Note that, in general, each wheel slips and skids while rolling. Some wheels will displace more or less than what they are assigned. These real wheel behaviours are summarised in the 12 patterns, as shown in Fig. 4. For instance, pattern (11) in the figure shows wheel positions (denoted by P_i and P_i') before and after a small motion. Also, S_i indicates the expected wheel goal when there is no slipping or skidding. Each pattern represents a candidate for different wheel destinations. However, it is difficult to determine an appropriate pattern for individual wheel because it is always determined on the basis of the interactive motion of all four wheels (see Fig. 5). Therefore, the trajectory of the robot's centre is not expressed in an algebraic form, and we trace the trajectory as a continuous path by iterating specific mathematical procedures by increasing each wheel angle incrementally.

Let us suppose that the robot stands on ζ_0 by aligning P_c on the Z_o-axis and facing in the Y_0-direction (see Fig. 6). Furthermore, imagine that each wheel rolls the distance l_i that is equal to $R_i \omega_i \Delta t$ without any disturbance. Then, the expected wheel position $S_i(x_i, y_i, z_i)$ in Σ is combined with P_{i0} in Σ_0, and we have the following coordinate relationships:

$$\begin{pmatrix} x_{si} \\ y_{si} \\ z_{si} \\ 1 \end{pmatrix} = \mathrm{Rot}(X, \theta_s)\mathrm{Trans}(a, b, 0)\mathrm{Rot}(Z, -\alpha) \begin{pmatrix} x_{i0} \\ y_{i0} + l_i \\ z_{i0} \\ 1 \end{pmatrix}$$
$$= \begin{pmatrix} x_{i0}\cos\alpha + (y_{i0} + l_i)\sin\alpha + a \\ \{-x_{i0}\sin\alpha + (y_{i0} + l_i)\cos\alpha + b\}\cos\theta_s - z_{i0}\sin\theta_s \\ \{-x_{i0}\sin\alpha + (y_{i0} + l_i)\cos\alpha + b\}\sin\theta_s - z_{i0}\cos\theta_s \\ 1 \end{pmatrix}. \quad (1)$$

Of course, l_i is zero when the robot locks wheel i from rolling.

Similarly, $P_i'(x_i', y_i', z_i')$ after each wheel rolls independently on ζ is combined with $P_{i0}(x_{i0}, y_{i0}, z_{i0})$ using the variations of (a_e, b_e) and α_e. That is, transformation parameters are $(a + a_e, b + b_e)$ and $\alpha + \alpha_e$ in turn of (a, b) and α in Eq. (1). Also, it is true that $z_{i0}' - z_{i0} = 0$ on the same plane ζ_0. Accordingly,

$$x_i' = x_{i0}\cos(\alpha + \alpha_e) + (y_{i0} + l_i)\sin(\alpha + \alpha_e) + a + a_e, \quad (2)$$

$$y_i' = \{-x_{i0}\sin(\alpha + \alpha_e) + (y_{i0} + l_i)\cos(\alpha + \alpha_e) + b + b_e\} \cos\theta_s - z_{i0}\sin\theta_s, \quad (3)$$

https://doi.org/10.1017/S026357471100035X Published online by Cambridge University Press

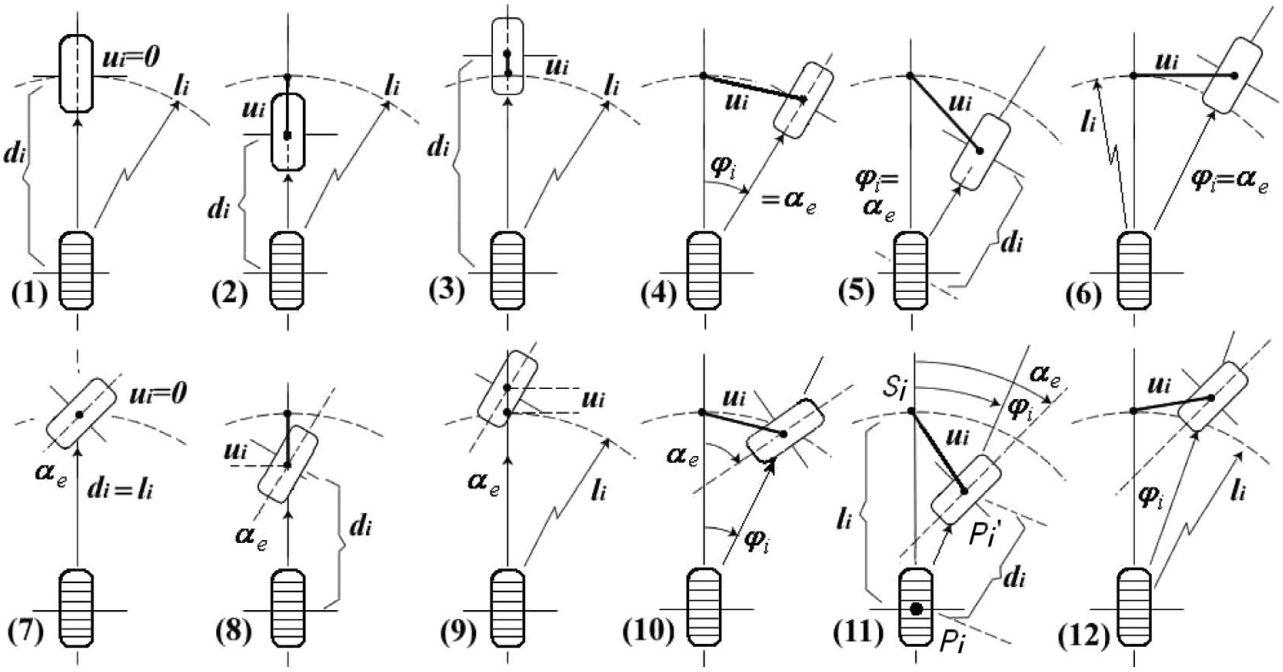

Fig. 4. Possible patterns of wheel movement combined with twisting and translation. Hatched and normal rectangles show the wheels before and after a small displacement, respectively.

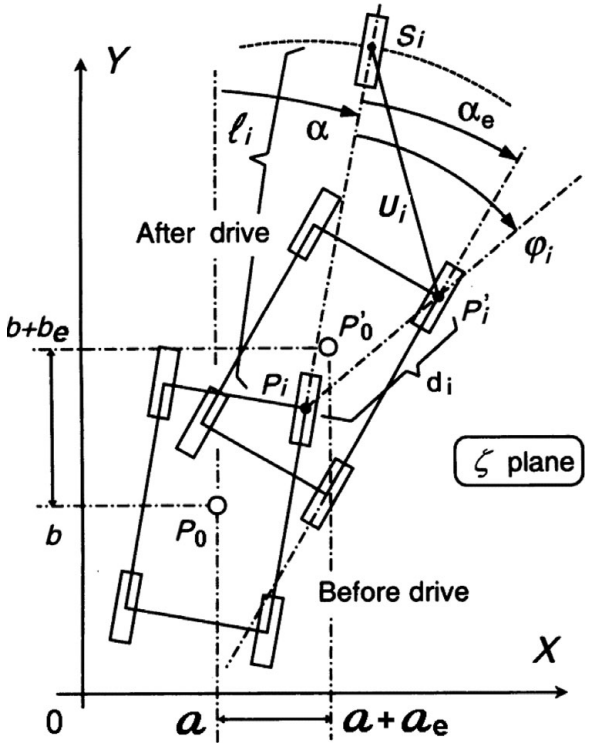

Fig. 5. Bottom view of a robot before and after a short time on the ground surface λ in the coordinate system $\Sigma(X, Y)$.

$$z_i' = \{-x_{i0}\sin(\alpha+\alpha_e) + (y_{i0}+l_i)\cos(\alpha+\alpha_e) + b + b_e\}\sin\theta_s - z_{i0}\cos\theta_s. \quad (4)$$

It is difficult to determine the weight distribution of the total weight to each wheel in contact with the ground when more than four wheels touch the ground, in general. Since our robot model is compliant meaning that all four wheels

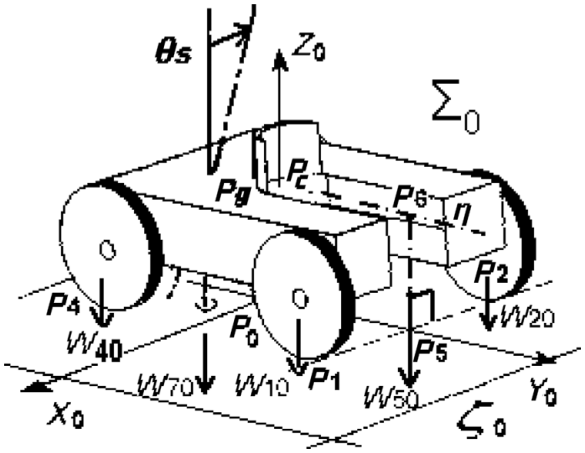

Fig. 6. Standing posture of a robot on the plane ζ_0.

are always in contact with the ground, we can assume that the front and rear parts of the robot body are able to twist freely around the η-axis that extends straight forward from P_c in the robot body (see Figs. 6 and 7). In addition, first we consider the line $\overline{(P_5P_6)}$ to make a virtual wheel touch at the point P_5 so that the total weight is shared among the three points P_3, P_4 and P_5. Then, we distribute the weight at P_5 over the actual points P_1 and P_2 by forming a moment balance at P_5. This is our method for determining the weight distributed at each of the four wheels.

We now have the following equations describing static equilibrium:

$$Wt = W_3 + W_4 + W_5 = W_{10} + W_{20} + W_{30} + W_{40}, \quad (5)$$

$$W_5 = W_1 + W_2, \quad (6)$$

https://doi.org/10.1017/S026357471100035X Published online by Cambridge University Press

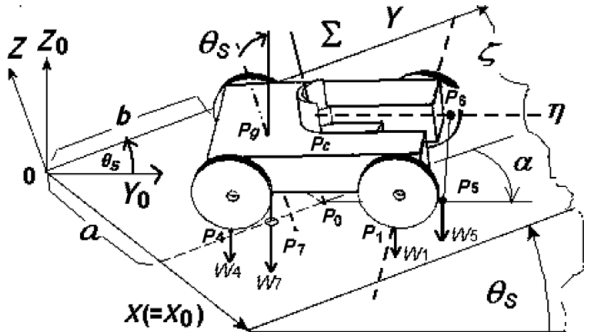

Fig. 7. Robot, as shown in Fig. 6, stands on the plane ζ after a coordinate transformation with the parameters (a, b) and α.

$$0 = \overrightarrow{P_g P_6} \times W_5 + \overrightarrow{P_g P_3} \times W_3 + \overrightarrow{P_g P_4} \times W_4, \tag{7}$$

$$0 = \chi \overrightarrow{P_6 P_1} \times W_1 + (1 - \chi)\overrightarrow{P_6 P_2} \times W_2. \tag{8}$$

The parameter χ depends on the twist angle (say $\pm\phi$) of the front body around the virtual axis η from the rear body. This appears when the ground surface is not flat in order to change the load balance between W_1 and W_2. In fact, the body adapts to have contact at P_1 and P_2 by determining P_5 depending on the compliance of the robot body. Therefore, we define the parameter χ as a function of ϕ. That is, $\chi = 0.5 + K_0\phi$, where K_0 is a twisting compliance factor of the front body in the range $0 < \chi < 1$. Note that χ takes the value 0.5 when the body can twist freely, i.e. $K_0 = 0$. A larger value of K_0 shifts P_5 towards P_1 or P_2 depending on W_3 and W_4. Solving these vector equations (seven unknowns with seven independent equations) yields the unknown position P_5 and each value from $W_1 - W_5$ at the state described by (a, b) and α in Fig. 7.

4. Evaluation of Energy Cost for Moving

4.1. Cost of motion caused by wheel twist

We estimate the energy cost of motion caused by a wheel twist using factors, such as μ_{di}, A_i, W_i and magnitude of velocity. The wheel contacts the ground with a rectangular tread, and its area changes if the wheel material is elastic. Therefore, the cost is strongly dependent on W_i, in general. However, if the wheel is made up of a hard material, the area can be assumed to be constant, and therefore, the pressure in the area will be invariant with respect to the contacting position. That is, $W_i = t_{ai} t_{bi}\ \tau$, where τ is a pressure in a unit. Then, we have the expression

$$\begin{aligned} E_{1i} &= \int_0^{\alpha_e} \int_{-t_{bi}/2}^{t_{bi}/2} \int_{-t_{ai}/2}^{t_{ai}/2} \mu_{di}\tau(x^2 + y^2)\,\mathrm{d}x\,\mathrm{d}y\,\mathrm{d}\theta \\ &= \left(t_{ai}^2 + t_{bi}^2\right)\mu_{di}|\alpha_e|W_i\ \cos\theta_s/12. \end{aligned} \tag{9}$$

This equation reveals that the energy cost is proportional to both W_i and α_e.

4.2. Cost of motion caused by wheel translation

Figure 4 shows the displacement of each wheel in contact with the ground. Note that U_i is desirable to be small enough within a same time elapse because the length stands for imaginary amount of power for dragging. Also, due to viscosity for driving wheels, the power of dragging is supposed to be proportional to the speed of completion ($=V_i$). Therefore, using a constant c, we can formulate the energy cost of a translation

$$E_{2i} = \mu_{di}\ U_i\ c|V_i|W_i\ \cos\theta_s. \tag{10}$$

It follows that

$$\begin{aligned} U_i c|v| &= U_i c|U_i/\Delta t| = U_i^2/\Delta t \\ &\equiv K U_i^2. \end{aligned} \tag{11}$$

For a powered wheel, this expression can be written as

$$\begin{aligned} U_i^2 &= (x_0' - x_{si})^2 + (y_0' - y_{si})^2 + (z_i' - z_{si})^2 \\ &= a_e^2 + C_{1i}\cos\alpha_e\, a_e + C_{2i}\sin\alpha_e a_e + C_{3i} a_e \\ &\quad + b_e^2 + C_{4i}\cos\alpha_e\, b_e + C_{5i}\sin\alpha_e b_e + C_{6i} b_e \\ &\quad + C_{7i}\cos\alpha_e + C_{8i}\sin\alpha_e + C_{9i}, \end{aligned} \tag{12}$$

where $C_{1i} - C_{9i}$ are defined as follows:

$$\begin{aligned} C_{1i} &= 2(x_{i0}\cos\alpha + y_{i0}\sin\alpha), \\ C_{2i} &= -2(x_{i0}\sin\alpha - y_{i0}\cos\alpha), \\ C_{3i} &= -2\{x_{i0}\cos\alpha + (y_{i0} + l_i)\sin\alpha\}, \\ C_{4i} &= C_{2i}, \qquad C_{5i} = -C_{1i}, \\ C_{6i} &= -C_{2i} - 2l_i\cos\alpha, \\ C_{7i} &= (C_{1i}C_{3i} + C_{2i}C_{6i})/2, \\ C_{8i} &= 2x_{i0}l_i, \\ C_{9i} &= 2\left(x_{i0}^2 + y_{i0}^2\right) + l_i(2y_{i0} + l_i). \end{aligned}$$

Finally, Eq. (10) can be written in a simplified manner as

$$E_{2i} = W_i\ \mu_{di}\ K\ U_i^2\cos\theta_s. \tag{13}$$

The exact value of μ_{di} is difficult to assign because of its variability in an actual environment. However, considering another constant, e, then μ_{di} in Eqs. (9), (10) and (13) can be expressed (as discussed in ref. [15]) as follows:

$$\mu_{di} = (1 - e\,v_i)\mu_{si}. \tag{14}$$

In particular, not only v_i, but also d_i have small magnitudes in our analysis. Then, μ_{di} is assumed to be a smaller constant than μ_{si}. This implies that a faster motion is estimated using a smaller value of μ_i. Henceforth, we use μ_i in place of μ_{di}. Practical values are reported in ref. [16], for instance.

4.3. Cost of climbing against gravity

A change in potential energy can be evaluated as

$$\begin{aligned} E_{3i} &= W_i(z_i' - z_i) \\ &= W_i\sin\theta_s(C_{2i}\cos\alpha_e - C_{1i}\sin\alpha_e + 2b_e - C_{2i})/2. \end{aligned} \tag{15}$$

https://doi.org/10.1017/S026357471100035X Published online by Cambridge University Press

Then, the total energy cost, E_t, using a constant K is

$$\begin{aligned} E_t &= \sum_{i=1}^{4} \{E_{1i} + E_{2i} + E_{3i}\} \\ &= \sum \left[\left\{\left(t_{ai}^2 + t_{bi}^2\right)/12\mu_i|\alpha_e| \cos\theta_s + \mu_i K U_i^2 \cos\theta_s \right. \right. \\ &\quad \left. \left. + (z_i' - z_i)\right\} W_i\right] \\ &= a_e(\lambda_1 a_e + \lambda_2 \cos\alpha_e + \lambda_3 \sin\alpha_e + \lambda_4) + b_e(\lambda_5 b_e \\ &\quad + \lambda_6 \cos\alpha_e + \lambda_7 \sin\alpha_e + \lambda_8) + \lambda_9 \cos\alpha_e \\ &\quad + \lambda_{10} \sin\alpha_e + \lambda_{11} + \lambda_{12}|\alpha_e|, \end{aligned} \tag{16}$$

where

$$\lambda_1 = K \cos\theta_s \sum_{i=1}^{4} \{W_i \mu_i\}, \tag{17}$$

$$\lambda_2 = K \cos\theta_s \sum \{W_i \mu_i\, C_{1i}\}, \tag{18}$$

$$\lambda_3 = K \cos\theta_s \sum \{W_i \mu_i C_{2i}\}, \tag{19}$$

$$\lambda_4 = K \cos\theta_s \sum \{W_i \mu_i\, C_{3i}\}, \tag{20}$$

$$\lambda_5 = \lambda_1, \tag{21}$$

$$\lambda_6 = \lambda_3, \tag{22}$$

$$\lambda_7 = -\lambda_2, \tag{23}$$

$$\lambda_8 = \sum [W_i\{K\mu_i \cos\theta_s\, C6_i + \sin\theta_s\}], \tag{24}$$

$$\begin{aligned} \lambda_9 = \sum [W_i\{K\mu_i \cos\theta_s (C_{1i}C_{3i} + C_{2i}C_{6i}) \\ + C_{2i} \sin\theta_s\}/2], \end{aligned} \tag{25}$$

$$\lambda_{10} = \sum [W_i\{K\mu_i \cos\theta_s C8_i - C_{1i} \sin\theta_s/2\}], \tag{26}$$

$$\lambda_{11} = \sum [W_i\{K\mu_i \cos\theta_s C_{9i} + C_{6i} \sin\theta_s/2\}], \tag{27}$$

$$\lambda_{12} = \sum \left\{W_i \mu_i \cos\theta_s \left(t_{ai}^2 + t_{bi}^2\right)/12\right\}. \tag{28}$$

5. Minimisation of Energy Cost

Interactive motion of four wheels as a mixture of slipping and skidding generates a resultant movement on a flat ground, including a slope. Estimating the motion is equivalent to solving for the unknown parameters (a_e, b_e) and α_e. On the basis of this consideration, we differentiate Eq. (16) with respect to the parameters (a_e, b_e) and α_e to find their values making E_t minimal for an actual movement based on the principle of virtual work

$$\partial E_t/\partial a_e = 2\lambda_1 a_e + \lambda_2 \cos\alpha_e + \lambda_3 \sin\alpha_e + \lambda_4 = 0, \tag{29}$$

$$\partial E_t/\partial b_e = 2\lambda_5 b_e + \lambda_6 \cos\alpha_e + \lambda_7 \sin\alpha_e + \lambda_8 = 0, \tag{30}$$

$$\begin{aligned} \partial E_t/\partial \alpha_e = &-(\lambda_2 \sin\alpha_e - \lambda_3 \cos\alpha_e)a_e \\ &-(\lambda_6 \sin\alpha_e - \lambda_7 \cos\alpha_e)b_e \\ &-(\lambda_9 \sin\alpha_e - \lambda_{10} \cos\alpha_e - \lambda_{12}) = 0. \end{aligned} \tag{31}$$

Inserting a_e in Eq. (29) and b_e in Eq. (30) into Eq. (31) yields an equation, including only the unknown parameter α_e. However, it is difficult to solve the fourth-order equation of α_e, in general. Therefore, we assume that $\alpha_e \approx 0$ so that $\sin\alpha_e \simeq \alpha_e$, $\cos\alpha_e \simeq 1$ and $\alpha_e^2 \simeq 0$. This reasonable approximation yields the following solution:

$$a_e = -(\lambda_2 cos\alpha_e + \lambda_3 \sin\alpha_e + \lambda_4)/(2\lambda_1), \tag{32}$$

$$b_e = -(\lambda_6 cos\alpha_e + \lambda_7 \sin\alpha_e + \lambda_8)/(2\lambda_5), \tag{33}$$

$$\alpha_e = \frac{\lambda_1\{\lambda_7\lambda_{68} - 2\lambda_5(\lambda_{10} + \lambda_{12})\} + \lambda_3\lambda_5\lambda_{24}}{\lambda_1\{\lambda_6\lambda_{68} - 2\lambda_5\lambda_9 - \lambda_7^2\} + \lambda_2\lambda_5\lambda_{24} - \lambda_3^2\lambda_5}, \tag{34}$$

where λ_{24} and λ_{68} are short notations for $\lambda_2 + \lambda_4$ and $\lambda_6 + \lambda_8$, respectively. Subsequent wheel positions are introduced repeatedly by replacing the old values of the parameters (a, b), and α with the new values $(a + \alpha_e, b + b_e)$, and $\alpha + \alpha_e$ to connect position histories in order to form a continuous trajectory.

6. Simulation of Robot Movement

Using the analysis above for minimizing the energy cost, simulating a robot's motion is possible.[17] Iterative calculation in the simulation program produces a continuous trajectory by connecting the transitional positions of the robot using the following algorithm:

(1) Assign the robot's dimensional specifications L_h, L_w, R_i, W_t, A_i, η, ω_i and Δt. Also, θ_s needs to be specified, in addition to μ_i. In this case, these values are obtained from the experimental setup using the PEOPLER-II robot.[14] That is, $L_h = 63$ cm, $L_w = 78$ cm, $R_i \simeq 20.7$ cm, $W_t = 107$ kg, $A_i = 1.0 \times 2.0$ cm^2 and $\Delta t = 0.1$ s. The constants μ_i, K and χ take 0.6, 1.0 and 0.5, respectively, in this paper, except for the simulation under hypothetical conditions.
(2) Locate the robot on the home ground to assign $P_{i0}(i = 1-4)$ on ζ_0. Then, assign $l_i(i = 1{-}4)$ by $R_i\omega_i\Delta t$, and apply the coordinate transformation using the parameters (a, b) and α, and $l_i(i = 1{-}4)$ to obtain $S_i(i = 1{-}4)$ on ζ.
(3) Likewise, locate the robot on the home ground again and apply the coordinate transformation using the parameters $(a + a_e, b + b_e)$ and $\alpha + \alpha_e$ to obtain $P_i'(i = 1{-}4)$ as a goal position of each wheel on ζ.
(4) Calculate the wheel load $W_i(i = 1-4)$ through the intrinsic weight W_5 operating at the virtual wheel contact at P_5.
(5) Calculate the parameters $C_{1i} - C_{9i}$ to determine the square of U_i.
(6) Calculate the parameters $\lambda_1 - \lambda_{10}, \lambda_{12}, \lambda_{24}$ and λ_{68} to evaluate E_t in Eq. (16).
(7) Solve the equation to obtain (a_e, b_e) and α_e, and determine $P_i'(i = 1{-}4)$ on ζ for the goal after incrementing θ_i to have l_i.
(8) Save the goal position as history on the way. Then, repeat the procedure from step 2, by replacing the values of (a, b) and α, with $(a + a_e, b + b_e)$ and $\alpha + \alpha_e$, respectively.

https://doi.org/10.1017/S026357471100035X Published online by Cambridge University Press

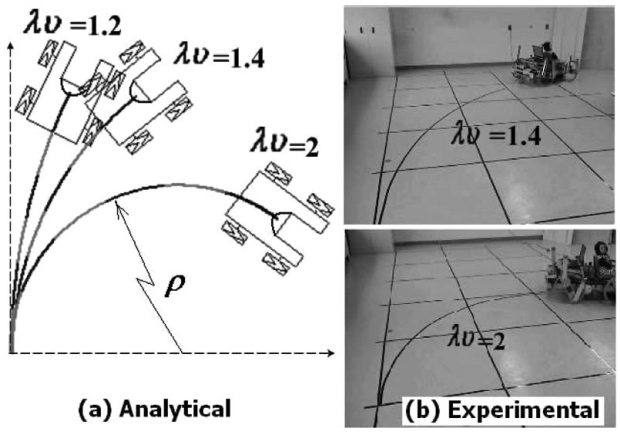

Fig. 8. Comparison of analytical and experimental results for turning.

To implement the above algorithm, we developed a program written in C^{++} and determined the trajectory on a ground surface with different values of $\mu_i, \theta_s, \lambda_v$. Figure 8a shows the simulation results for turning with $\lambda_v = 1.2$, 1.4 and 2.0 on a tile floor. Same calculations are made with robots having different aspect ratios. However, trajectories resulted in comparable forms and sizes, and consequently, they are not included in this paper.

7. Experimental Results in Various Conditions

We conducted several experiments to investigate the influence of friction coefficients, payload distribution and slope angle of the ground on the resulting robot motion. For these experiments, we used the PEOPLER-II robot on horizontal tile and wooden floors, including a sloped wooden mock-up with $\theta_s = 6°$. Black tape is pasted on the floor to establish 1 m × 1 m grids for taking a global measure. When measuring the weight distribution to each wheel on the home ground, we found that $W_{10} = 23$ kg, $W_{20} = 18$ kg, $W_{30} = 36$ kg and $W_{40} = 30$ kg with $\phi \simeq 0$. Values of μ_i are collected experimentally. That is, 0.295 and 0.268 on p-tile and wooden floors, respectively.

7.1. Fundamental motion of rolling straight

The robot rolls straight forward/backward using $\lambda_v = 1$ when $R_i (i = 1 - 4)$ are all the same. This is true even when the wheel radii are not equal, as long as $l_i (i = 1–4)$ are all the same. If the wheels rotate in opposite directions in the front and back, the robot remains at its current position. Trajectory estimation in these cases is not needed because the trajectory is just a straight line going forward/backward, or a stationary point from an analytical viewpoint. These results were proven in both analytical and experimental results. In particular, on a slope, the robot moved down gradually depending on θ_s while moving forward/backward. These results are not included in this section because the next section showing a spinning motion proves these characteristics.

7.2. Specific motion for changing travelling direction

7.2.1. Turning. In general, the robot turns when $\lambda_v \neq -1$. Analytical and experimental results generated on the p-tile with $\mu_i = 0.295$ are shown in Fig. 8. In the figure, trajectories are concerned with a set of positions P_{mc} collected by the marker-C (see Fig. 1). The location of this marker was attached to the robot with a shift backward by 4.0 cm from P_0 because a driving motor occupied the central area of the robot body. We conducted the experiment for λ_v values of 1.4 and 2. Figure 9 shows sequential photos of the robot turning with $\lambda_v = 2.0$. These results show that the robot turns more sharply as λ_v increases and that the experimental trajectories are similar to those of the simulation. A quantitative analysis is shown in Table I, where the trajectories are compared with ρ of curves. From the comparison given in Table I, it is clear that the calculation algorithm is reasonable and effective for

Table I. Comparison of predicted and experimental turning trajectories.

Control λ_v	Simulation radius $= \rho_s$	Experimental radius $= \rho_e$	Error $(\rho_e - \rho_s)/\rho_e$
1.4	1.94 m	2.05 m	0.0537
2.0	4.10 m	4.23 m	0.0307

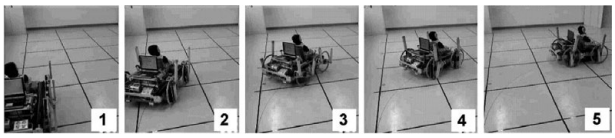

Fig. 9. Sequential photos of turning motion, as shown in Fig. 8b.

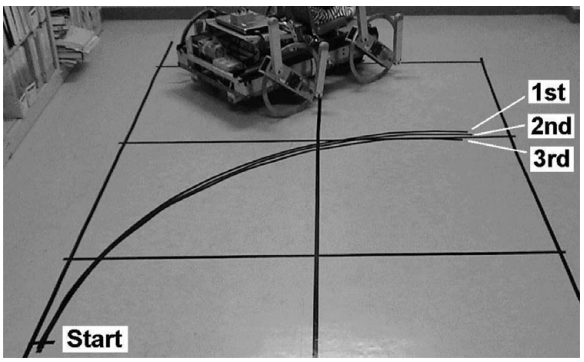

Fig. 10. Repetitively collected trajectories of turning with $\lambda v = 2.0$ on the tile floor.

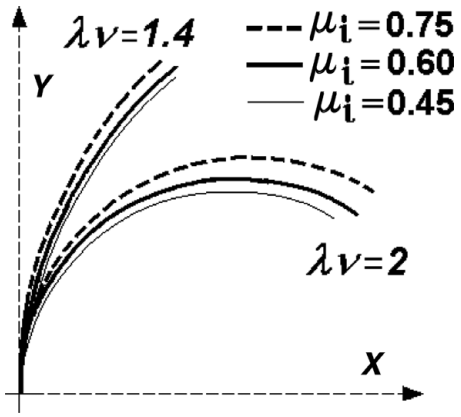

Fig. 11. Simulated trajectories of turning under different μ_i on a floor.

https://doi.org/10.1017/S026357471100035X Published online by Cambridge University Press

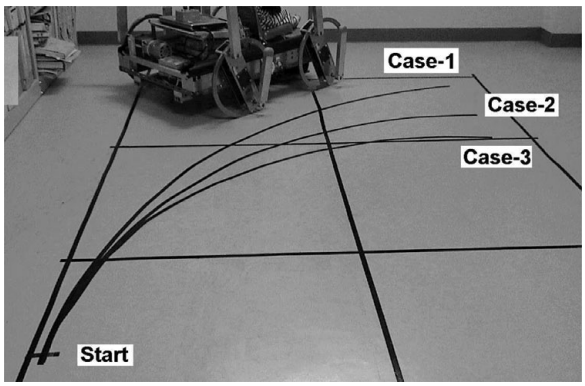

Fig. 12. Experimental trajectories when a robot turns with different speeds keeping λ_v same to 2.0 on the tile floor.

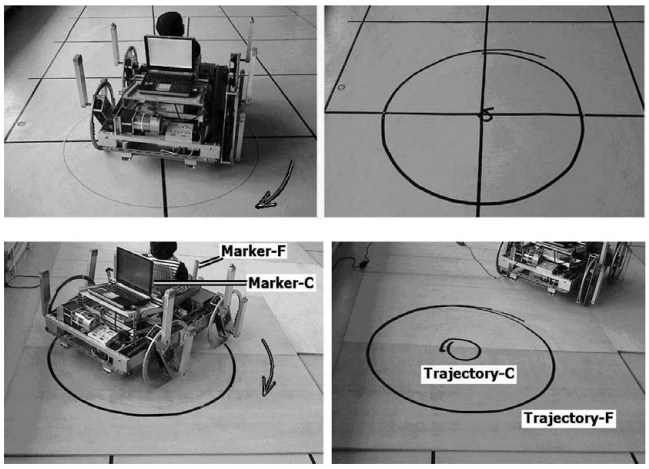

Fig. 13. Experimental validation of spinning. Top and bottom bird's-eye views are on p-tile and wooden floors, respectively. Outer and inner trajectories relate to positions of P_{mf} and P_{mc}, respectively.

estimating a robot trajectory to within about 5.4%. Figure 10 shows experimental trajectories obtained by repeating the turning on the p-tile with $\lambda_v = 2.0$. Clearly, three results are very much alike to prove reproducibility.

In the analysis, trajectories of a turn are influenced by μ_i. For instance, Fig. 11 shows the influence when λ_v is 1.4 and 2.0. Also, ν_i is supposed to be a small and only λ_v is considered. Therefore, robot's speed is not reflected on the simulation algorithm in exact sense. However, experimental trajectories are collected when the speed changes with keeping λ_v same. Actually, Fig. 12 shows the results in Case 1: $\nu_2 = 2.87$ rpm, Case 2; $\nu_2 = 3.67$ rpm and Case 3: $\nu_2 = 6.28$ rpm with $\lambda_v = 2.0$. From the figure, it is evident that the trajectory in Case 3 is high in turning performance. This is understandable by the fact that the robot can turn easily with a small value of μ_i, that is when ν_2 increases.

7.2.2. Spinning. The robot spins when $\lambda v = -1$. This motion is beneficial for changing the direction of travel while remaining at the same location. Figure 13 shows the experimental results of this type of spin executed by the robot on p-tile and wooden floors. Inner curves are drawn by the marker-C tracing P_{mc}. Likewise, outer curves are drawn by the marker-F that is set 55.0 cm forward from P_c. Diameters of 123.1 cm and 109.5 cm are measured on the outer trajectories in top and bottom photos. Those of inner trajectories are 5.1 cm and 19.1 cm. These results show that COG becomes easy to move when μ_i decreases. Therefore, inner circle on the wooden floor became larger and outer circle became smaller. On the p-tile, characteristics of these diameters are opposite because the coefficient of friction on p-tile is greater than on wood. These differences are confirmed also by simulation results that are not shown in this paper for conciseness.

When the robot spins on the sloped wooden mock-up, simulation of motion for P_{mc} and P_{mf} resulted in the curves, as shown in Fig. 14a. In the simulation, COG is fixed but W_t is distributed to each wheel depending on θ_s and α. Experimental trajectories of P_{mc} and P_{mf} are shown in Figs. 14b and 14c. The robot travels down the slope from the top to the bottom, as seen in the figure. Comparing the predicted and experimental trajectories confirms that the robot does indeed have a tendency to move down the slope while spinning. Table II shows the quantitative errors evaluated by measuring the distances of SMF_{max}, SMC_{min}, SMF_{min} and SMC_{max} (see Fig. 14a). From these data, we can confirm that the analytical and experimental results are very similar by comparing simulated and experimental trajectory curves. Figure 15 shows spinning trajectories that

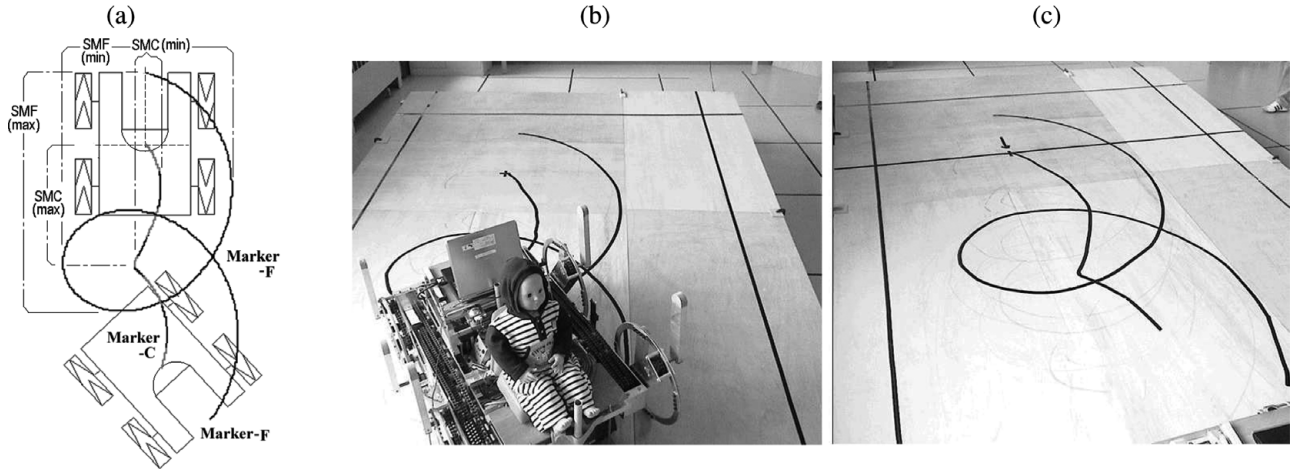

Fig. 14. Simulated results and experimental results on a sloped wooden mock-up. Top and bottom of the figure show high and low levels of the slope. The robot itself blocks part of trajectory trace in (b) and is removed from the scene in (c).

https://doi.org/10.1017/S026357471100035X Published online by Cambridge University Press

Table II. Comparison of predicted and experimental spinning trajectories.

Attribute	Simulation D_{sim}	Experimental D_{exp}	Error $(D_{exp} - D_{sim})/D_{exp}$
SMF_{max}	176.7 cm	181.0 cm	+0.024
SMF_{min}	126.9 cm	113.8 cm	−0.115
SMC_{max}	89.4 cm	105.0 cm	+0.149
SMC_{min}	22.2 cm	21.1 cm	−0.052

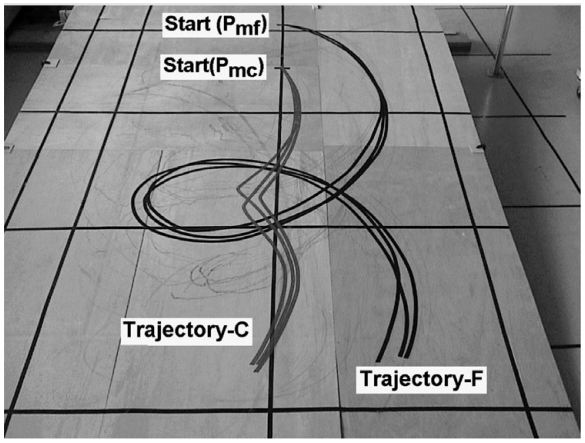

Fig. 15. Repetitively collected trajectories of spinning with $\lambda v = -1$ on the sloped wooden mock-up.

are collected by a same control on the sloped wooden mock-up. The photos show that the trajectory is reproducible in shape and size when a ground condition is constant. It is considered that a small trajectory error is caused by a wooden unevenness in hardness since stamped area became harder to change the coefficient of friction.

8. Conclusion

We proposed a mathematical formulation based on virtual work for evaluating the energy cost of a variety of robot motions combined with slipping and skidding. Minimizing the sum of the virtual work expressions resulted in a solution for the predicted motion of wheeled robot. We then simulated motion of a robot while rolling and steering using both turning and spinning on a flat ground and a sloped surface. The hybrid robot PEOPLER-II was used to generate experimental trajectories on tile and wooden floors using control rules similar to those used in the simulations. The predicted and experimental data showed analogous trajectory forms with an error as small as 5.4% in turning and 14.9% in spinning. The mathematical formulation is applicable to simulate robot motion in a variety of environmental conditions according to various needs, such as those of vehicle users, designers and programmers, without manoeuvring an actual machine. Simulation results can be used to better understand how the trajectories of 4WDSSMRs are produced.

Our future research aim is to provide a helpful display of a trajectory so that a driver can trace an assigned route easily. In this navigation system, the relationships between λ_v and ρ might be built-in as a database, and appropriate data might be selected by a driver, or two-axis gravity direction sensors and visual sensors that are helpful to automatically predict the upcoming trajectory.

Acknowledgements

This work was partially supported by Kakenhi Grant (No.21560259), provided by the Japan Society for the Promotion of Science (JSPS). The author Abeer Mahmoud also received support from her country Egypt.

References

1. F. Asano and Z.-W. Luo, "Asymptotically stable biped gait generation based on stability principle of rimless wheel," *Robotica* **27**, 949–958 (2009).
2. S. Han, B. Choi and J. Lee, "A precise curved motion planning for a differential driving mobile robot," *Mechatronics* **18**, 486–494 (2008).
3. Z. Shiller and Y.-R. Gwo, "Dynamic motion planning of autonomous vehicles," *IEEE Trans. Robot. Autom.* **7**(2), 241–249 (1991).
4. M. Nitulescu, "Theoretical Aspects in Wheeled Mobile Robot Control," *Proceedings of the IEEE International Conference on Automation, Quality and Testing, Robotics*, Cluj-Napoca (May 2008) vol. 2, pp. 331–336.
5. C. B. Low and D. Wang, "Integrated Estimation for Wheel Mobile Robot Posture, Velocities, and Wheel Skidding and Slipping Perturbations," *Proceedings of the IEEE/RSJ Internatinal Conference on Intelligent Robots and Systems (IROS)*, Nice, France (Sep. 2008) pp. 20–30.
6. L. Caracciolo, A. D. Luca and S. Iannitti, "Trajectory Tracking Control of a Four-Wheel Differentially Driven Mobile Robot," *Proceedings of the IEEE International Conference on Robotics and Automation*, Detroit, Michigan (May 1999) pp. 2632–2638.
7. D. Wang and C. B. Low, "Modeling and analysis of skidding and slipping in wheeled mobile robots: Control design perspective," *IEEE Trans. Robot.* **24**(3), 676–687 (2008).
8. R. Balakrishna and A. Ghosal, "Modeling of slip for wheeled mobile robots," *IEEE Trans. Robot. Autom.* **11**(1), 126–132 (1995).
9. H. Chitsaz, S. M. Lavalle, D. J. Balkcom and M. T. Mason, "Minimum wheel-rotation paths for differential-drive mobile robots," *Int. J. Rob. Res.* **28**(1), 66–80 (2009).
10. D. B. Reister and F. G. Pin, "Time-optimal trajectories for mobile robots with two independently driven wheels," *Int. J. Rob. Res.* **13**(1), 38–54 (1994).
11. M. A. Minor, B. W. Albiston and C. L. Schwensen, "Simplified motion control of a two-axle compliant framed wheeled mobile robot," *Int. Trans. Robot.* **22**(3), 491–506 (2006).
12. T. Okada, A. Mahmoud and W. Botelho, "Trajectory Analysis of an Independently Driven Wheeled Robot and It's Experimental Verification," *Proceedings of the 12th International Conference on Climbing and Walking Robots (CLAWAR)*, Istanbul, Turkey (Sep. 2009) pp. 781–790.
13. T. Okada, W. T. Botelho and T. Shimizu, "Compatible Use of a Legged Robot as a Wheeled Robot and Its Demonstrative Simulation," *Proceedings of the 9th International Conference on Climbing and Walking Robots (CLAWAR)*, Brussels, Belgium (Sep. 2006) pp. 34–44.

https://doi.org/10.1017/S026357471100035X Published online by Cambridge University Press

14. T. Okada, W. T. Botelho and T. Shimizu, "Motion analysis with experimental verification of the hybrid robot, PEOPLER-II, for reversible switch between walk and roll on demand," *Int. J. Rob. Res.* **29**(9), 1199–1221 (Aug. 2010).
15. H. Sakai, "Friction and wear of tire tread rubber," *J. Tire Science and Technology*, **24**(3), 252–275 (Jul. 1996).
16. H. Hotta, "On a friction coefficient of sliding on the ground," *Monthly Report of CERI*, **481**, 65–68 (1993) (in Japanese).
17. A. Mahmoud, T. Okada and T. Shimizu, "A simulation for estimating a circular trajectory of a rotating four-legged mobile robot on regular terrain," *J. Cybern. Syst.* **2**(1), 9–16 (Jun. 2009).

https://doi.org/10.1017/S026357471100035X Published online by Cambridge University Press